Yang *et al. Biochar* (2024) 6:46
https://doi.org/10.1007/s42773-024-00338-x

Biochar

ORIGINAL RESEARCH Open Access

A novel biochar-based 3D composite for ultrafast and selective Cr(VI) removal in electroplating wastewater

Zongzheng Yang[1,2†], Jinjin Wang[1†], Nan Zhao[3], Runyi Pang[1], Chuanfang Zhao[6], Ying Deng[1], Di Yang[1], Haochen Jiang[2], Zhiguo Wu[1,2*] and Rongliang Qiu[4,5*]

Abstract

In this study, a newly developed composite of biochar-poly(*m*-phenylenediamine) (BC-P*m*PD) exhibiting a distinct skeletal structure was synthesized for the purpose of extracting Cr(VI) from aqueous solutions. BC was employed as a supportive carrier onto which P*m*PD nanoparticles were uniformly affixed through *in-situ* polymerization and oxidation synthesis, both within and outside the layered configuration of BC. The structural stability and morphologies of BC-P*m*PD were assessed utilizing Fourier transform infrared (FTIR) spectroscopy, scanning electron microscopy, thermogravimetric analysis, analysis of specific surface area and pore size, X-ray photoelectron spectroscopy (XPS), and X-ray diffraction. In comparison to other modified BCs reported, BC-P*m*PD exhibited the highest Cr(VI) removal rate. Specifically, at 303 K, BC-P*m*PD achieved a maximum Cr(VI) removal capacity of 775 mg g^{-1}, surpassing the capabilities of unmodified BC and P*m*PD by 10.4 and 2.13 times, respectively. Analyses involving XPS, FTIR, and density functional theory calculation confirmed that proton transfer happened between protonated amine ($-NH_2$) functional group within the structure of BC-P*m*PD and $HCrO_4^-$ before the formation of hydrogen bond. Subsequently, environmentally persistent free radicals facilitated the reduction of the adsorbed Cr(VI). Quantification of the functional groups indicated that the amino group was responsible for 93.0% of the Cr(VI) adsorption in BC-P*m*PD. BC-P*m*PD displayed potent adsorption and reduction capabilities, alongside notable stability, repeatability, and promising potential for application in the remediation for high concentrations of Cr(VI) in electroplating wastewater scenarios.

Highlights

- Novel 3D material was prepared and the removal rate of Cr(VI) on BC-P*m*PD was the highest as compared to reported BCs.
- The maximum adsorption amount of Cr(VI) on BC-P*m*PD was high up to 1034 mg g^{-1} at 323 K and $-NH_2$ adsorbed 93.0% $HCrO_4^-$.
- DFT calculation confirmed proton transfer happened between protonated $-NH_2$ and $HCrO_4^-$ before the formation of H bond.

Handling editor: Xing Yang

†Zongzheng Yang and Jinjin Wang are the first co-authors.

*Correspondence:
Zhiguo Wu
wzhg@tust.edu.cn
Rongliang Qiu
eesqrl@mail.sysu.edu.cn
Full list of author information is available at the end of the article

Keywords BC-poly(*m*-phenylenediamine) composite, Selective removal of Cr(VI), Electroplating wastewater, Proton transfer, H bond

Graphical Abstract

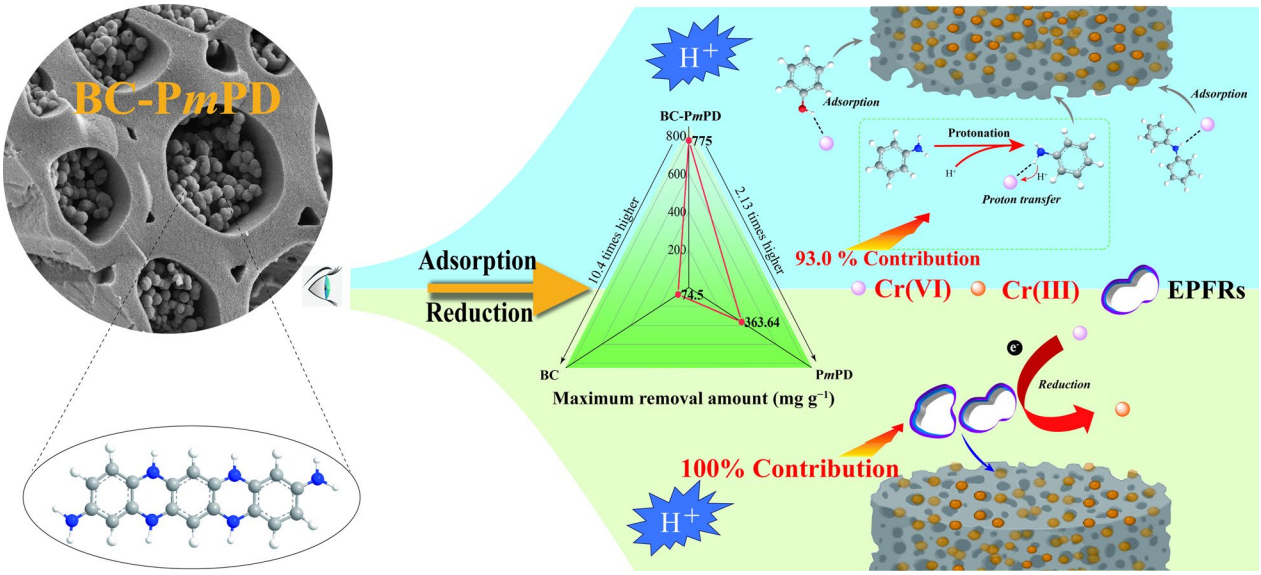

1 Introduction

Heavy metals are categorized by the World Health Organization as substances that are carcinogenic and toxic. Contamination from heavy metals such as As, Pb, Cr, Cd, and Hg, has resulted in serious health problems (Binish et al. 2022). Cr exists in two oxidation states: Cr(III) and Cr(VI). Among these, Cr(VI) is particularly hazardous to public health due to its mutagenic and carcinogenic properties (Hu et al. 2011). In China, wastewater containing Cr predominantly comes from various industries, including chemical production, electroplating, leather manufacturing, metallurgy, and pigment fabrication. Methods to remove Cr(VI) from water include precipitation, reduction, coagulation, flotation, and adsorption. Of these methods, adsorption is particularly promising due to its simplicity, high efficiency, and cost-effectiveness (Yang et al. 2018).

Biochar (BC) is identified as a carbon-rich biosorbent with a low production cost. It is manufactured through the pyrolysis of biomass at temperatures ranging from 300–700 °C under anoxic conditions (Zhao et al. 2022b). The material has garnered significant interest due to its inherent properties, including high cation exchange capacity, specific surface area, unique pore structure, and oxygen-rich functional groups (Sinha et al. 2022; Zou et al. 2021). It has the potential to reduce carbon emissions, which aligns with the pursuit of carbon neutrality (Zhu et al. 2022), and is conducive to advancing multiple United Nations Sustainable Development Goals (UN SDGs) and Environmental, Social, and Governance (ESG) objectives (Yuan et al. 2023). However, the adsorption capacity of unmodified BC for Cr(VI) in water remains limited (Asuquo et al. 2017). For instance, the maximum adsorption capacities of unmodified BC prepared from beet tailings and *Artemisia argyi* stems for Cr(VI) were 123 and 162 mg g^{-1}, respectively (Dong et al. 2011; Song et al. 2019). The negative charge associated with unmodified BC (Zhao et al. 2022a) could impede the adsorption of CrO_4^{2-} in aqueous solutions. Meanwhile, reduction happened during the decontamination of Cr(VI) (Xu et al. 2023, 2022). Thus, numerous researchers have focused on enhancing the adsorption and reduction performances of Cr(VI) by modifying BC through various methods. These methods include physical activation (Peng et al. 2018), acid treatment (Zhao et al. 2018), organic grafting (Song et al. 2021), metal impregnation (Shaheen et al. 2022), metal oxide loading (Zou et al. 2021), and magnetization modification (Sinha et al. 2022). The maximum adsorption capacity of polyethylenimine-alkali-modified BC for Cr(VI) reached approximately 436 mg g^{-1}. This value is approximately 18.9 times higher than the adsorption capacity of unmodified BC,

which is 23.1 mg g^{-1} (Ma et al. 2014). However, it should be noted that polyethylenimine is highly toxic and is not rapidly removed in the blood (Guo et al. 2023).

Poly(*m*-phenylenediamine) (P*m*PD), a diamine derivative of polyaniline, has attracted increasing attention for its superior environmental stability, reduced preparation cost, richer functional groups, and greater versatility compared to polyaniline. P*m*PD has found applications in various fields, such as electrodes, sensors, actuators, and catalysis (Cao et al. 2017; Yang et al. 2018). The polymer demonstrates significant potential for removing heavy metals from aqueous solutions. Its maximum adsorption capacities are 243 mg g^{-1} for Pb(II) and 1.92 g g^{-1} for Ag(I), respectively (Huang et al. 2007; Li et al. 2004). P*m*PD has also shown considerable adsorption capacity for Cr(VI), with the maximum removal reported as 526 mg g^{-1} at pH 2 and 25 °C (Kera et al. 2018). Compared to commonly used metal modification methods such as nanoscale zero-valent iron (Qian et al. 2023) available in the market, P*m*PD is less expensive and does not introduce other metal impurities into the aqueous solution. It also does not pose environmental risks. Additionally, the rich functional groups present in P*m*PD can adsorb Cr(VI) and reduce it to Cr(III) (Chen et al. 2019). However, P*m*PD tends to form agglomerated spherical structures, which limits the exposure of its functional groups to contaminants (Hao et al. 2021). Prior studies have attempted to improve the adsorption of Cr(VI) by combining P*m*PD with materials like calcium fibers, cobalt or zirconium-based metal organic frameworks, and reduced graphene oxide. These combinations promote the efficient removal of Cr(VI) mainly by increasing ionic strength and facilitating mechanisms like electrostatic adsorption, redox reactions, and chelation. In acidic conditions, aniline groups (-–NH–) in P*m*PD are protonated, thereby attracting Cr(VI) through electrostatic adsorption. They are also oxidized by Cr(VI), resulting in the formation of new quinone imines (–N=) and Cr(III) (Cao et al. 2017; Jin et al. 2018; Wang et al. 2020).

Despite these advancements, existing composites have not proven to be specifically selective and practical for the removal of Cr(VI) in real-world wastewater scenarios. BC, with its three-dimensional (3D) honeycomb network structure, can serve as a carbon carrier for P*m*PD to reduce agglomeration. It is hypothesized that the substantial specific surface area and porosity provided by BC facilitate enhanced loading of P*m*PD, thereby augmenting its capacity for adsorption–reduction of Cr(VI). To date, no literature exists on the use of P*m*PD-loaded BC for the improved adsorption and reduction efficiency of Cr(VI) in wastewater. The removal mechanism also remains undefined. Considering these factors, the objectives of this paper are: (1) to prepare a novel 3D composite material by combining BC with P*m*PD particles (BC-P*m*PD); (2) to study the kinetics, isotherm, and thermodynamics of Cr(VI) adsorption by BC-P*m*PD; (3) to elucidate the mechanism of Cr(VI) removal on BC-P*m*PD through Fourier Transform infrared spectroscopy (FTIR), X-ray photoelectron spectroscopy (XPS), electron spin resonance (ESR) and density functional theory (DFT) calculation; and (4) to evaluate the recycling performance and the efficiency of high-concentration Cr(VI) removal in actual electroplating-contaminated wastewater by BC-P*m*PD.

2 Materials and methods

2.1 Synthesis of BC and BC-P*m*PD

Corn stover obtained from a farm in Jixian District, Tianjin, was thoroughly washed with tap water and dried in an electronic air blast drying oven (DGG-101–0, Tianjin Tianyu) for 24 h at 105 °C. The dried corn stover was crushed in a mill, and then pyrolyzed in a Muffle furnace (YB-1700A, Luoyang Navit) at 500 °C for 4 h under oxygen-free conditions. After cooling to room temperature, BC was obtained, and it was ground to a particle size range of 0.05–1.5 mm for further use.

The synthesis of BC-P*m*PD composites is depicted in Fig. 1 Under ice bath conditions, 3 g of *m*-phenylenediamine (*m*PD) monomer was weighed and placed in a 250 mL beaker, to which 100 mL of deionized water was added and stirred to dissolve. Then, 0.1 g of BC was added to the above solution and stirred for 2 h. Subsequently, 6.61 g of sodium persulfate was added as an oxidant. At the same time, the prepared 30 mL solution of Na_2CO_3 with a concentration of 2 mol L^{-1} in a 50 mL syringe was slowly injected into the beaker at a rate of 2 mL min^{-1}. Following this, the solution was mechanically stirred at 400 rpm min^{-1} for 5 h. At the end of the reaction, the mixture was poured into a sand core funnel for vacuum filtration, and the sample solution was sequentially washed to neutrality with deionized water, 1:1 (v:v) ammonia water, and deionized water to eliminate residual ions and monomers. Finally, the samples were cleansed with absolute ethanol to remove the oligomers, and then dried in a vacuum freeze-drying oven at −60 °C for 12 h. The effects of preparation conditions for BC-P*m*PD on Cr(VI) removal were investigated to obtain the optimal adsorption material and the details are shown in supporting information (Additional file 1: Fig.S1).

2.2 Removal experiments

The adsorption kinetic experiments were conducted in a triangular flask containing 250 mL of Cr(VI) solution (300, 500, and 700 mg L^{-1}) and 0.1 g of BC-P*m*PD. The

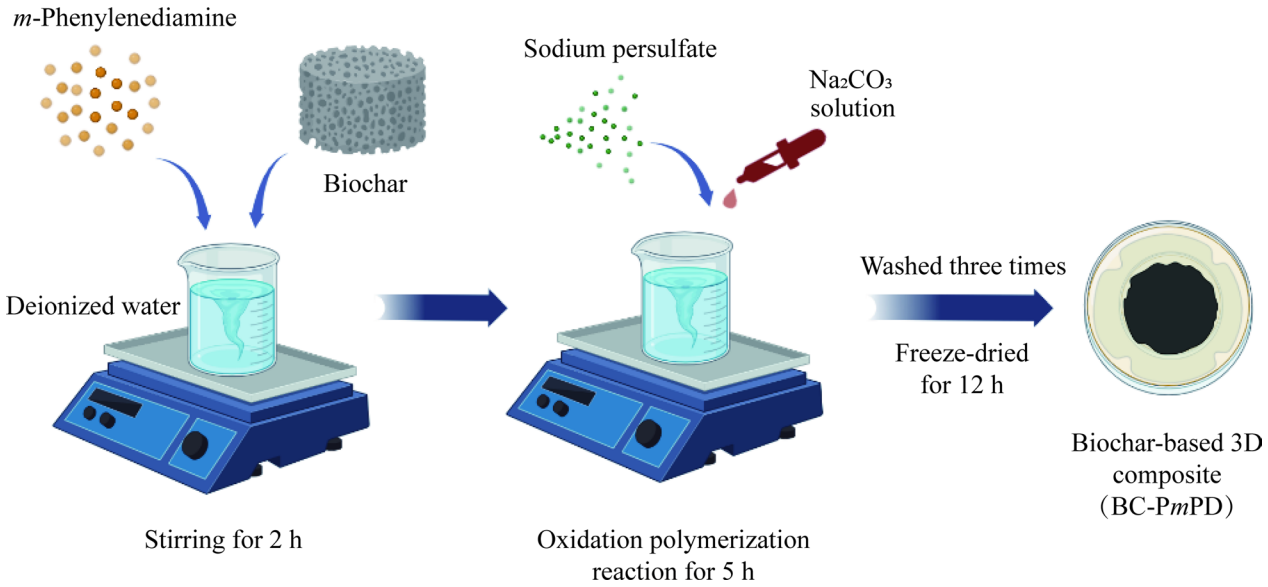

Fig. 1 Schematic diagram of BC-P*m*PD preparation process

flask was placed in a vibrating shaker (150 rpm) at 30 °C. After a designated adsorption time (0–24 h), the samples were filtered using a 0.45 μm membrane filter. The fitting equations for kinetics, isotherms, and thermodynamic models are listed in the Supporting Information.

The effects of BC-P*m*PD on Cr(VI) adsorption under different conditions were investigated by altering the initial solution pH (2–10), concentration (200–1000 mg L^{-1}), temperature (5–55 °C), and the presence of common ions (Mg^{2+}, Co^{2+}, Cd^{2+}, Cu^{2+}, Zn^{2+}, Cl^{-}, NO_3^{-}, SO_4^{2-}, and PO_4^{3-}). All of these experiments were repeated three times. Solution pH measurements were performed with a pH meter (FE20, Mettler Toledo, Shanghai, China). The concentration of Cr(VI) was determined using 1,5-diphenylhydrazine spectrophotometry. Inductively coupled plasma mass spectrometry (Walsam, UK) was employed to ascertain the concentrations of total Cr and other coexisting metal ions in the solution.

BC-P*m*PD with adsorbed Cr(VI) was desorbed in a 0.1 M sodium hydroxide solution and shaken for 8 h. Subsequently, the adsorbent was filtered and collected, washed to neutrality, dried to a constant weight, and then used for the next Cr(VI) removal cycle. After each equilibrium adsorption and prior to desorption, the concentrations of Cr(VI) and Cr(III) in the filtrate at different initial concentrations were determined. This cycle was repeated for 5 times.

The electroplating wastewater was obtained from a leather factory in Guangzhou, Guangdong Province. The organic carbon content was measured using an organic matter detector (CT1000B, Zhejiang, China), and its content was not high, approximately 2.14 mg L^{-1}. The concentration of Cr was 200 mg L^{-1}, while other metals such as Cd, Rb, Sr, Zr, Ni, and Zn were present at concentrations of 2.42, 1.47, 1.60, 2.09, 51.64, and 9.09 mg L^{-1}, respectively. The pH was approximately 2, indicating strong acidity.

2.3 DFT calculation for the interaction energy

In order to gain insight into the interactions of BC-P*m*PD with $HCrO_4^{-}$, computational studies were carried out. 4a,5,10,10a-tetrahydro-phenazine-2,7-diamine was chosen as model compound of N containing group. The structures of model compound and their $HCrO_4^{-}$ complexes were optimized with B3LYP (Becke 1993a, b; Lee et al. 1988; Stephens et al. 1994) method and 6-31G + (d,p) (Clark et al. 1983) basis set for nonmetal elements, C, H, O, N and LANL2DZ (Hay and Wadt 1985) basis set for metal element, $HCrO_4^{-}$. To get their thermodynamic parameters, frequency analyses were carried out at the same theoretical level on the optimized structures. The solvent effect was also considered by computing single point energy with B3LYP method and 6–311 + + G(d, p) (Feller 1996) basis set for nonmetal elements, SDD (Andrae et al. 1991) basis set for metal elements and PCM (Miertuš and Tomasi 1981) solvation model on each optimized structure. All the computations were performed with Gaussian 09 software (El-Barbary and Alkhateeb 2021). Their 3D molecule structures were drawn with CYLview (Legault 2009).

3 Results and discussion

3.1 Structural characteristics of BC and BC-P*m*PD

3.1.1 Scanning electron microscopy-energy dispersive spectroscopy (SEM–EDS) and electron donating capacities (EDCs) analysis

The SEM images of BC, P*m*PD, and BC-P*m*PD are presented in Fig. 2a–d, respectively. Figure 2a displays the initial carbon structure of BC, showing a typical thin and coarse multi-layer honeycomb carbon structure that is loosely dispersed, providing a 3D support skeleton for the attachment of P*m*PD nanoparticles. Figure 2b reveals the polymer morphology after the oxidation polymerization of *m*PD monomer, exhibiting fine circular nanoparticles in a dense and stacked state. In Fig. 2c, d hundreds to thousands of P*m*PD nanoparticles were observed on BC after modification, uniformly attached to the BC surface or embedded within BC interlayer pores. This phenomenon could be attributed to the fact that uneven and irregular sites on BC can strongly bind P*m*PD nanoparticles. Moreover, the −OH groups on BC promote the *in-situ* polymerization of BC and *m*PD, serving as a robust scaffold for P*m*PD nanoparticles and preventing their detachment from the BC surface (Yang et al. 2018). The apparent elemental changes in Table 1 and Additional file 1: Fig. S2a, b indicate the successful integration of P*m*PD into the BC backbone. Additionally, the O/C ratio changed little, signifying the polar oxygen-containing functional groups were kept after modification (Peng

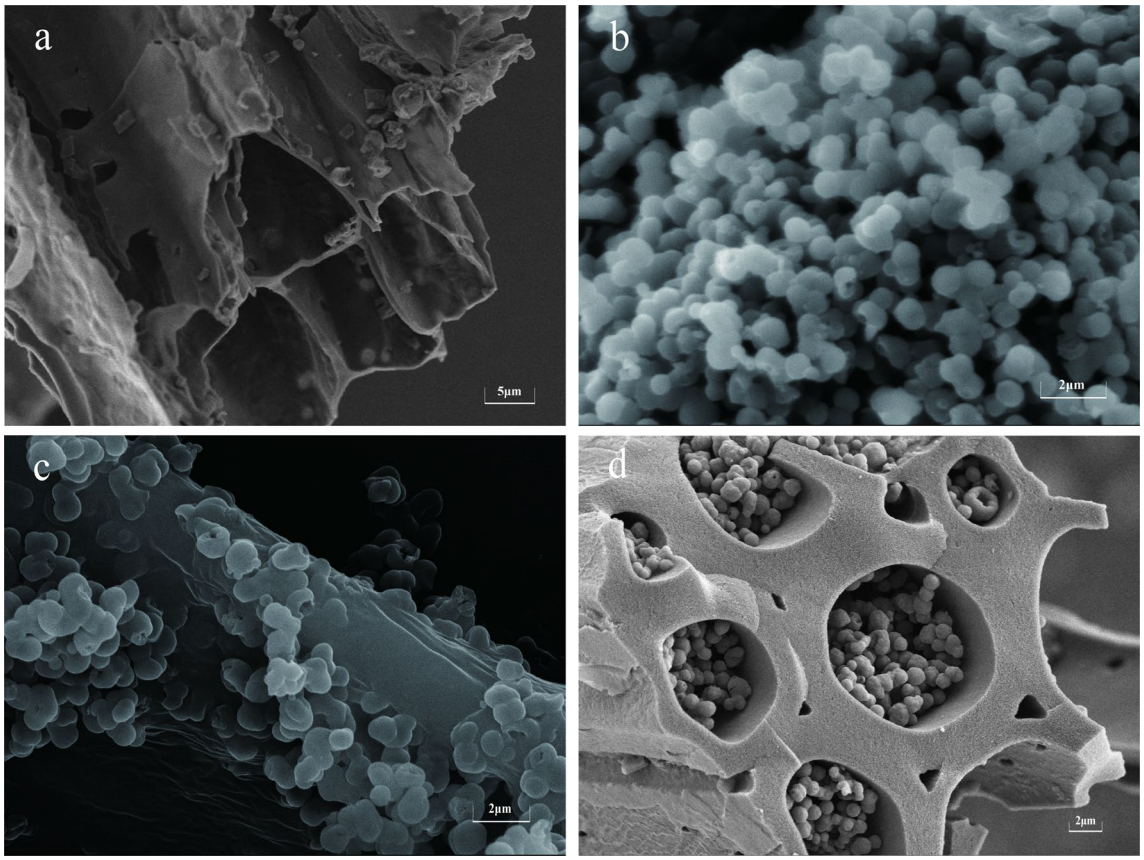

Fig. 2 The SEM images of **a** BC, **b** P*m*PD, and **c d** BC-P*m*PD. Note: The scale bars of **a** and **b-d** are 5 and 2 μm

Table 1 Chemical composition and EDC values of BC and BC-P*m*PD

Material	Element content (%)														O/C	EDC value ($mmol_{e^-}\ g^{-1}$)
	C	O	N	Cl	Mg	P	Na	Al	Si	S	K	Ca	Cu	Zn		
BC	74.68	10.62	0.00	0.66	0.97	1.02	0.04	0.00	4.10	0.46	5.88	1.56	0.01	0.00	0.14	0.21
BC-P*m*PD	71.43	9.67	17.04	0.15	0.09	0.33	0.20	0.00	0.05	0.87	0.12	0.03	0.00	0.02	0.13	0.56

Table 2 The BET and pore size of BC and BC-P*m*PD

Material	BET ($m^2\ g^{-1}$)	Pore volume ($cm^3\ g^{-1}$)	Pore size (nm)	Mesopore ratio
BC	76.3	0.051	10.3	68.7%
BC-P*m*PD	10.1	0.026	8.92	53.6%

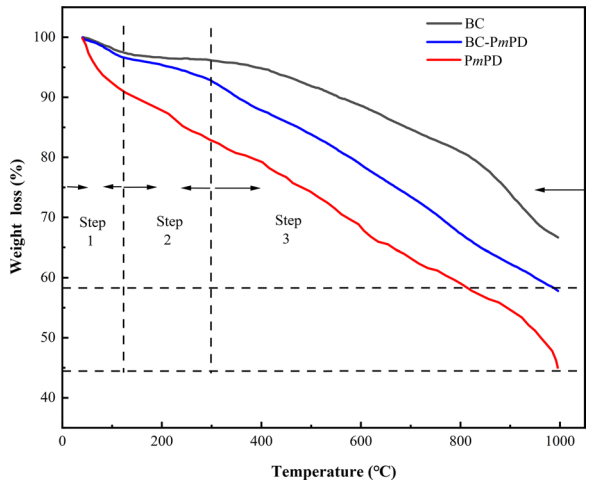

Fig. 3 The percentage of weight loss as a function of temperature for BC, P*m*PD, and BC-P*m*PD

et al. 2018). The EDC values of BC and BC-P*m*PD are 0.21 and 0.56 $mmol_{e-}\ g^{-1}$, respectively (Additional file 1: Fig. S3). The higher value of BC-P*m*PD indicated that the loading of P*m*PD also make it present higher reduction capacity (Chen et al. 2022; Xu et al. 2019a).

3.1.2 Brunauer–Emmett–Teller (BET) surface area and thermogravimetric (TGA) analysis

Upon loading P*m*PD nanoparticles, the specific surface area of BC decreased from 76.3 to 10.1 $m^2\ g^{-1}$, as shown in Table 2, suggesting that the multi-layer honeycomb structure of BC facilitated the loading of P*m*PD nanoparticles (Huang et al. 2007). The pore sizes and mesopore ratio of BC and BC-P*m*PD were 8.92–10.3 nm and 53.6–68.7%, respectively, indicating their mesoporous nature. The higher mesopore volume with smaller mesopore diameter can provide more active sites, rendering them suitable for liquid-phase adsorption and facilitating the adsorbate diffusion within the adsorbent (Asuquo et al. 2017).

The mass loss process of BC, P*m*PD, and BC-P*m*PD was studied by TGA when the temperature was raised to 1000 °C in the air atmosphere. As shown in Fig. 3, the first mass loss of BC, P*m*PD, and BC-P*m*PD about 1.60%, 8.11%, and 4.34% occurred when the temperature gradually increased to 110 °C, respectively, due to the evaporation of the water adsorbed by the material and a small amount of volatile substances (Stoica-Guzun et al. 2016). During the second pyrolyzation stage from 110 to 300 °C, a significant weight loss of 15.9% in P*m*PD was happened due to the loss of low molecular weight oligomers. After 300 °C, the unstable cellulose or some volatile thermal compounds in BC would disappear with the further increase of temperature (Tripathy et al. 2021). The mass loss of BC-P*m*PD at this stage was higher than that of BC, which may derive from the thermal decomposition of polymer due to molecular chain breakage at high temperature. When the temperature rose to 1000 °C, the final residual amounts of BC, P*m*PD, and BC-P*m*PD were 66.6%, 39.2%, and 57.8%, respectively. It can be seen that BC-P*m*PD can maintain a good thermal stability in air and has less mass loss.

3.1.3 Fourier transform infrared (FTIR)

Changes in the characteristic functional groups of the prepared BC, P*m*PD, and BC-P*m*PD were examined using FTIR, as shown in Fig. 4a. The distinct spectra illustrate alterations in the functional groups on the surface of the original BC and the BC loaded with polymer. The initial carbon structure of BC exhibits multiple functional groups, including −CH (2916 cm^{-1}), C=C (1590 cm^{-1}), O–H (3428 cm^{-1}), and CH_2 (1385 cm^{-1}) (Zhao et al. 2017). For P*m*PD, various bands of functional groups are evident, such as −NH− (3345 cm^{-1}), $-NH_2$ (3216 cm^{-1}), C=N (1614 cm^{-1}), C–N (1501 cm^{-1}, 1256 cm^{-1}), and C–O (1036 cm^{-1}) (Hao et al. 2021; Yang et al. 2018). A similar pattern to P*m*PD was observed in the BC-P*m*PD sample, with peaks at 1036, 1256, 1614, and 3345 cm^{-1}. The prominent enhancement of the characteristic peak at 1614 cm^{-1} confirms the successful loading of P*m*PD onto the original carbon structure of BC. Additionally, the relative increase in vibrational intensity of each characteristic peak in BC-P*m*PD indicates that the incorporation of BC enhances the content and stability of each polymer functional group. Notably, BC-P*m*PD exhibited a significant increase in the intensity of −NH− at 3345 cm^{-1} compared to P*m*PD. The −OH at 3428 cm^{-1} on BC shifted to a lower frequency of 3418 cm^{-1} upon combination with P*m*PD via wet chemical methods, resulting in BC-P*m*PD. These phenomena are possibly due to hydrogen bond formation between $-NH_2$ in P*m*PD and −OH in BC, affirming a strong interaction between BC and P*m*PD nanoparticles (Yang et al. 2018). Thus, P*m*PD has been successfully loaded onto BC via wet chemical methods.

3.1.4 X-ray diffraction (XRD)

The material's crystal structure was characterized using XRD. In Fig. 4b, both P*m*PD and BC-P*m*PD exhibit a

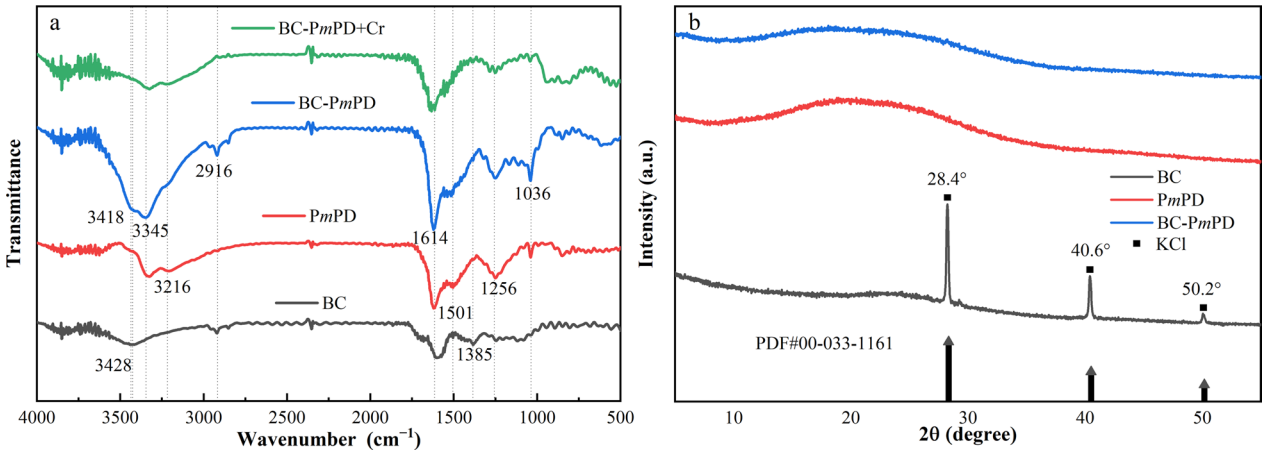

Fig. 4 **a** FTIR spectra of BC, P*m*PD, and BC-P*m*PD before and after Cr(VI) removal; **b** XRD spectra of BC, P*m*PD, and BC-P*m*PD powders

highly similar wide diffraction band, a characteristic feature of an amorphous structure (Ding et al. 2018). The XRD data of BC displayed diffraction peaks at 28.4°, 40.6°, and 50.2°, attributed to KCl (PDF#00-033-1161), confirming the typical components of bare BC. Notably, the BC-P*m*PD diffraction peak decreased compared to P*m*PD, possibly due to widened interlayer spacing and increased amorphous nature resulting from the modification (Wan et al. 2018). Furthermore, XRD patterns revealed a nearly complete disappearance of the diffraction peaks following the incorporation of P*m*PD into BC. This phenomenon can be attributed to the influence of P*m*PD nanoparticles on the surface structure and diffraction peak intensity of BC. And KCl might be dissolved during the loading of P*m*PD or the washing process. This indicates that the presence of P*m*PD nanoparticles affected the composition of BC and the intensity of diffraction peaks, corroborating the findings from XPS and FTIR.

3.2 Removal performance

3.2.1 Effect of pH on Cr(VI) removal

The speciation of Cr(VI) in aqueous solutions closely depends on pH (Kera et al. 2018). pH significantly influences the surface charge and functional groups of the adsorbent (Rafique et al. 2021). The Zeta potentials of BC and BC-P*m*PD are shown in Additional file 1: Fig. S4a and the BC and BC-P*m*PD surface were positively charged at pH = 2.0 (pH < BC (pH_{pzc}, 4.05) < BC-P*m*PD (pH_{pzc}, 5.37)). As depicted in Fig. 5a, BC-P*m*PD exhibited the highest Cr(VI) adsorption at pH 2, with an adsorption amount of 554 mg g^{-1}. This behavior may be attributed to the acidic nature of the solution at low pH, causing H^+ to interact with the lone pair of electrons on the amino group, resulting in polymer protonation. BC-P*m*PD is positively charged and electrostatically attracts the negatively charged $HCrO_4^-$ ions (the primary form of Cr(VI) in low pH solutions). Simultaneously, $HCrO_4^-$ readily accepts electrons for reduction to Cr(III) by BC-P*m*PD under acidic conditions (Dognani et al. 2019). Subsequently, Cr(VI) adsorption capacity declined as pH increased, reaching a minimum of 9.02 mg g^{-1} at pH ≥ 8. With increasing pH, increased concentration of OH^- compete for adsorption sites on the BC-P*m*PD surface. Additionally, the protonation of amino groups on the BC-P*m*PD structure diminishes, leading to electrostatic repulsion between Cr(VI) and the negatively charged BC-P*m*PD surface, contributing to the reduced Cr(VI) removal capacity (Albadarin et al. 2012). The reduction of Cr(VI) by BC-P*m*PD under different pH conditions was also observed (Additional file 1: Fig. S4b), and the concentration of Cr(VI) gradually decreased while Cr(III) increased in the aqueous solution at low pH conditions. This indicated that the produced Cr(III) on BC-P*m*PD was gradually released into the solutions. No Cr(III) was detected at pH 8 and 10, suggesting that high pH conditions are not conducive to the formation of Cr(III).

3.2.2 Effect of initial concentration and temperature on Cr(VI) removal

The efficiency of Cr(VI) removal decreased with an increase in the initial concentration of Cr(VI) from 200 to 1000 mg L^{-1} at the optimum pH of 2, as depicted in Fig. 5b. It remained high, up to 90%, for initial concentrations below 800 mg L^{-1}. For Cr(VI) concentrations of 800 and 1000 mg L^{-1}, the removal efficiencies decreased to 87.8% and 51.6%, respectively. The likelihood of collision between Cr(VI) and the adsorbent was greater for low concentrations of the Cr(VI) solution because a higher driving force was present to overcome the mass transfer

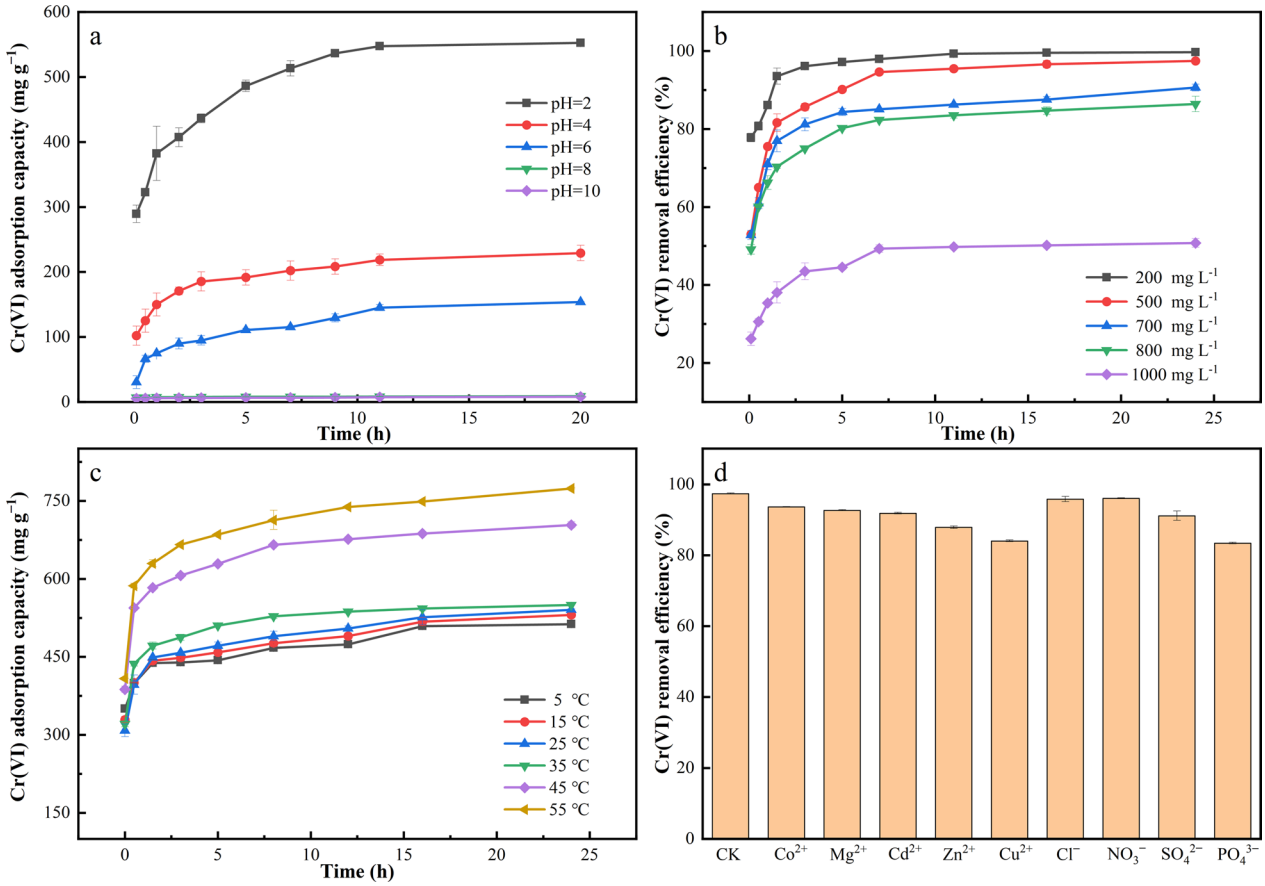

Fig. 5 Effects of different conditions on the performances of Cr(VI) removal by BC-P*m*PD: **a** Different initial solution pH (2, 4, 6, 8, and 10), **b** Concentrations (200, 500, 700, 800, and 1000 mg L^{-1}), **c** Temperatures (5, 15, 25, 35, 45, and 55 °C), **d** Coexisting ions (Co^{2+}, Mg^{2+}, Cd^{2+}, Zn^{2+}, Cu^{2+}, Cl^{-}, NO_3^{-}, SO_4^{2-}, and PO_4^{3-}) (Conditions: BC-P*m*PD dosage = 1 g L^{-1}, pH = 2, T = 30 °C, t = 24 h)

resistance of the adsorbent during the adsorption process (Cao et al. 2017). The significant decrease in Cr(VI) removal efficiency for solution concentrations above 800 mg L^{-1} is due to the occupation and saturation of all available active sites for adsorption on the adsorbent surface (Liu et al. 2019). When the experimental temperature increased from 5 to 55 °C (Fig. 5c), the adsorption amount of Cr(VI) increased from 493 to 774 mg g^{-1}, indicating that the adsorption of Cr(VI) by BC-P*m*PD in an aqueous solution is an endothermic process.

3.2.3 Effect of coexisting ions on Cr(VI) removal

In reality, most wastewater contains a variety of coexisting ions, making it important and necessary to study the selective adsorption behavior of Cr(VI) on BC-P*m*PD under conditions of coexisting ions. Metal cations (Mg^{2+}, Co^{2+}, Cd^{2+}, Cu^{2+}, and Zn^{2+}) and anions (Cl^{-}, NO_3^{-}, SO_4^{2-}, and PO_4^{3-}) at 500 mg L^{-1} concentration were mixed with the $HCrO_4^{-}$ solution, respectively. Figure 5d indicates that the presence of other coexisting ions (Mg^{2+}, Co^{2+}, Cd^{2+}, Cl^{-}, NO_3^{-}, SO_4^{2-}, and PO_4^{3-}) in the solution had no significant effect on the removal of Cr(VI) by BC-P*m*PD. Cu^{2+} and Zn^{2+} caused a slight decrease in adsorption capacity, indicating that they inhibit Cr(VI) adsorption by competing for adsorption sites on BC-P*m*PD and depleting the surface sites (Wang et al. 2015b). However, the average adsorption amount was still maintained at a very high level of 441 mg g^{-1}, possibly because the positive charge on the surface of BC-P*m*PD after amino protonation did not attract and adsorb metal cations. Meanwhile, the presence of the coexisting PO_4^{3-} in the solution led to a slight decrease in adsorption capacity, probably because the interaction force between PO_4^{3-} and the adsorption site of BC-P*m*PD might be stronger than that between $HCrO_4^{-}$ in the solution (Bhaumik et al. 2012). However, $HCrO_4^{-}$ had a high positive redox potential and was still relatively easy to reduce to Cr(III) by BC-P*m*PD. According to Additional file 1: Fig. S5a, the changes in the concentration of each metal cation in the solution before and after the reaction were not significant, and the Cr(III) concentrations in the solution were reduced after the addition

of metal cations (Additional file 1: Fig. S5b), suggesting that no ion exchange reaction happened. The reduction of $HCrO_4^-$ concentration in the solution before and after the reaction was very significant and this indicated that BC-P*m*PD can efficiently and selectively remove Cr(VI) from wastewater (Cao et al. 2017; Xu et al. 2019b).

3.3 Adsorption kinetics and isotherm

3.3.1 Adsorption kinetics

The Cr(VI) adsorption kinetics experiments were conducted at three different initial concentrations, and the removal of Cr(VI) by the adsorbent as a function of contact time is shown in Fig. 6a–c. The removal rate of Cr(VI) by BC-P*m*PD was very fast in the first 2 h, and the removal efficiency reached 80%. The removal showed a slow increasing trend after 2 h and reached adsorption equilibrium at around 8 h. The pseudo first-order kinetic model exhibited lower correlation coefficient values, indicating poor linearization (Table 3). The q_e value obtained by this model significantly differed from the experimental value, implying that the reaction could not be categorized as a first-order reaction. The correlation coefficients for the pseudo-secondary kinetic model were all greater than 0.999, and the calculated q_e values matched well with the experimental data (Zhang et al. 2018). Therefore, the experimental results suggested that Cr(VI) removal occurred through a chemical reaction with the functional groups of BC-P*m*PD, involving electron sharing or exchange to achieve adsorption. Various studies on the kinetics of Cr(VI) adsorption for different adsorbents have also reported the high relevance of the pseudo-secondary kinetic model (Liu et al. 2023; Zhao et al. 2021b). The R^2 value in the Elovich model exceeded 0.939, indicating that the Cr(VI) removal process involved diffusion, activation, and adsorption on the surface of BC-P*m*PD. The calculated maximum removal rate of 700 mg L^{-1} Cr(VI) on BC-P*m*PD in Table 3 was remarkably high at 2002 mg $(g\ min)^{-1}$, which was 221 and 575 times higher than those of mangosteen shells and N-rich biochars, respectively (Shan et al. 2020; Zhao et al. 2021b). The results suggested that the adsorption rate of Cr(VI) by BC-P*m*PD was exceedingly fast (refer to

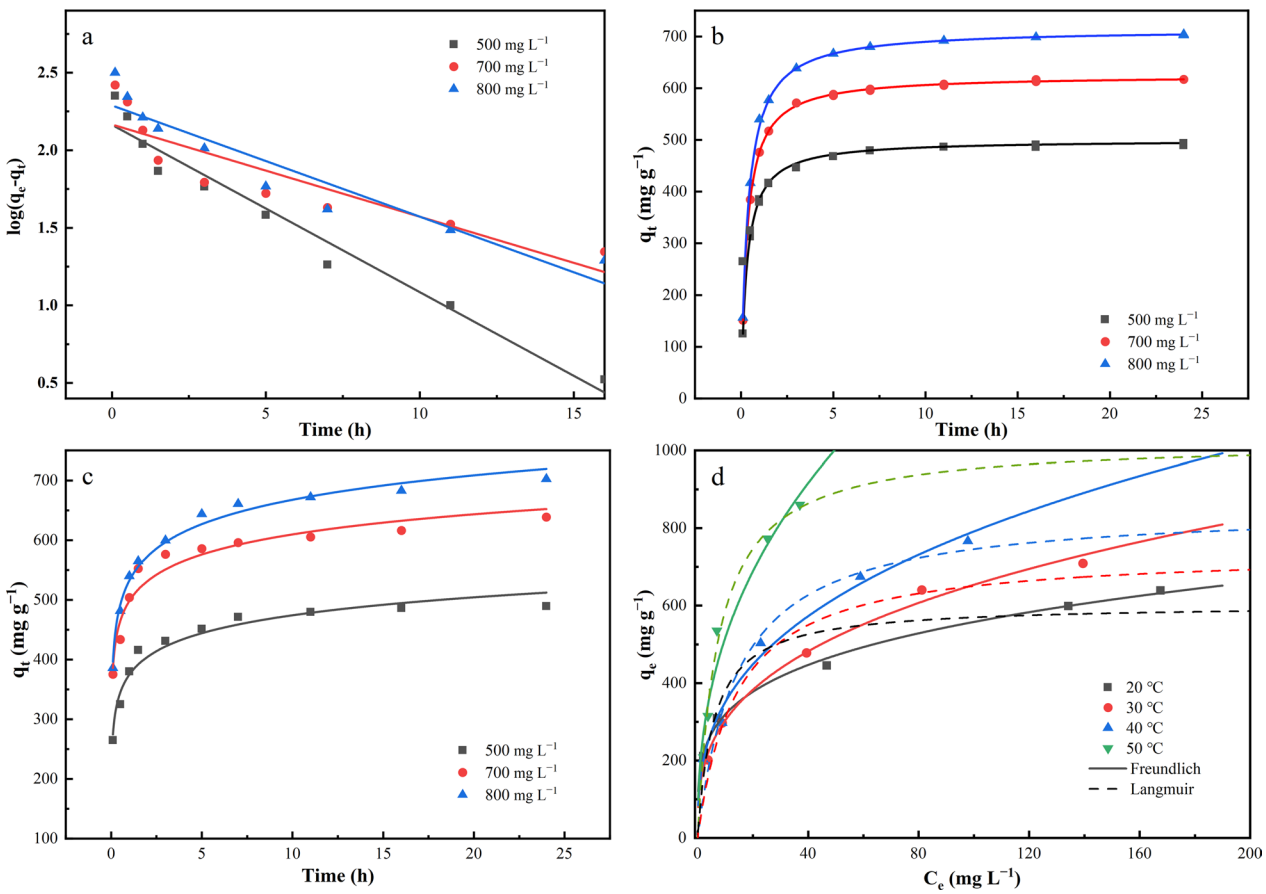

Fig. 6 The adsorption of Cr(VI) on BC-P*m*PD: **a** Pseudo-first-order kinetic model, **b** Pseudo-second-order kinetic model, **c** Elovich model (Concentrations = 500, 700, and 800 mg L^{-1}, pH = 2, T = 30 °C, t = 24 h); **d** Langmuir and Freundlich adsorption isotherms (Concentrations = 200–800 mg L^{-1}, pH = 2, T = 20, 30, 40, and 50 °C, t = 24 h)

Table 3 Adsorption kinetics simulation parameters of Cr(VI) on BC-P*m*PD

C_0 (mg L^{-1})	Pseudo first-order			Pseudo-second-order			Elovich			
	q_e (mg g^{-1})	K_1 (min^{-1})	R^2	q_e (mg g^{-1})	K_2 (g(mg $min)^{-1}$)	V_0 (mg (g $min)^{-1}$)	R^2	a (mg g^{-1} min^{-1})	b (g min^{-1})	R^2
500	146	0.248	0.958	495	0.0066	1608	0.999	374	43.3	0.957
700	147	0.137	0.771	625	0.0051	2002	0.999	498	48.6	0.939
800	194	0.165	0.884	714	0.0039	1998	0.999	532	58.9	0.984

$V_{0=} q_e^2 K_2$, R^2 is correlation coefficient

Table 4 Adsorption isotherm simulation parameters of Cr(VI) on BC-P*m*PD

Temperature (K)	Langmuir			Freundlich		
	q_{max} (mg g^{-1})	K_L (L mg^{-1})	R^2	n	K_F (mg (g (L $mg^{-1})^n)^{-1}$)	R^2
293	697	0.056	0.987	3.23	133	0.949
303	775	0.063	0.988	3.01	141	0.988
313	850	0.077	0.984	2.83	156	0.980
323	1034	0.128	0.996	2.33	190	0.956

Supplementary Movie), making BC-P*m*PD a promising material.

3.3.2 Adsorption isotherm

The study of adsorption isotherms is important for determining the adsorption effect. According to the experimental data obtained through linear regression analysis, the Langmuir model in Fig. 6d shows a higher correlation compared to the Freundlich model within the studied concentration range. The parameters of the isotherms are summarized in Table 4, and the highest values of K_L and q_{max} reached 0.128 L mg^{-1} and 1034 mg g^{-1} at 323 K. Both K_L and q_{max} increase with rising temperature, indicating that the binding of heavy metals to the active sites of the adsorbent is enhanced at higher temperatures. This suggests that the adsorbent is homogeneous in terms of binding sites for monolayer adsorption (Al-Ghouti and Da'ana 2020). This result is consistent with the adsorption findings of Cr(VI) by other P*m*PD and BC materials. Additionally, the q_{max} value of BC-P*m*PD was significantly higher than that reported for magnetic nanoporous carbon poly(*m*-phenylenediamine) (Gao et al. 2021), *calotropis gigantea* fiber oxidation poly(*m*-phenylenediamine) (Cao et al. 2017), and bacterial cellulose/P*m*PD (Yang et al. 2018) at similar temperatures, as shown in Additional file 1: Table S1.

3.4 Thermodynamic studies

Thermodynamic consideration of the adsorption process is necessary to conclude whether the process is spontaneous. Negative values of Gibbs free energy (ΔG) were investigated to confirm the feasibility of the process and the spontaneity of adsorption. As the temperature increased from 293 to 323 K, the negative value of ΔG also increased, indicating that higher temperature favored the heat absorption reaction (Gao et al. 2021). The standard enthalpy (ΔH) and entropy (ΔS) of adsorption, as fitted by Additional file 1: Fig. S6, are 46.4 kJ mol^{-1} and 168 J K^{-1} mol^{-1}, respectively, with a correlation coefficient of 0.97. Values of thermodynamic calculation parameters are presented in Table 5. A positive ΔH value suggests that the adsorption process of Cr(VI) by BC-P*m*PD is an endothermic reaction, and the positive ΔS value reflects an increase in disorder at the solid–liquid interface during the adsorption process.

Table 5 Thermodynamic parameters for Cr(VI) adsorption on BC-P*m*PD

Temperature (K)	K_C (mL g^{-1})	ΔG (kJ mol^{-1})	ΔH (kJ mol^{-1})	ΔS (J K^{-1} mol^{-1})	R^2
293	3.70	−3.06			
303	5.78	−4.42			
313	9.44	−5.84			
323	24.1	−8.19	46.4	168	0.97

3.5 Removal mechanism of Cr(VI)

The removal mechanism of Cr(VI) on BC-P*m*PD was analyzed using FTIR technique. As shown in Fig. 4a, the peaks corresponding to −NH−, −OH, C=N, C−N, and

C-O functional groups significantly decrease, indicating the involvement of these functional groups in Cr(VI) removal.

Further analysis of BC-P*m*PD samples before and after adsorption using XPS was performed to study the removal mechanisms. In Fig. 7a, C 1 s, N 1 s, and O 1 s peaks are observed at 284 eV, 399 eV, and 531 eV in BC-P*m*PD, respectively. After the adsorption reaction, a typical Cr 2p peak at 578 eV appeared, providing further evidence for the adsorption of Cr(VI) on the surface of BC-P*m*PD. High-resolution XPS spectra of Cr 2p after the adsorption of Cr(VI) by BC-P*m*PD are shown in Fig. 8b, displaying two asymmetric bands: Cr 2p1/2 and Cr 2p3/2 and these bands are fitted to form Cr(VI) (587.5 eV, 578.8 eV) and Cr(III) (586.7 eV, 577.0 eV). By calculating the percentage of Cr(VI) and Cr(III) on BC-P*m*PD, it was found that 73.4% of adsorbed Cr(VI) on BC-P*m*PD was reduced to Cr(III). Moreover, Cr(III) was detected in varying concentrations of Cr(VI) solution after reaction (Additional file 1: Fig. S7), suggesting simultaneous adsorption and reduction of Cr(VI) (Wang et al. 2015a).

The atomic percentage of N 1 s decreased, indicating the involvement of N-containing groups in Cr(VI) removal. N-containing functional groups can provide or share their lone electron pairs with other ions carrying empty orbitals (Tian et al. 2015). The N 1 s spectrum of BC-P*m*PD was divided into two peaks: −NH− (399.3 eV) and −N=(398.8 eV) (Fig. 7c, d). An additional peak of −N=$^{+}$ appeared at 401.2 eV after the reaction of BC-P*m*PD with acidic aqueous solution, likely due to the protonation reaction. After adsorption, the −NH− and −N=peak areas decreased from 64.3% to 52.4%, and 35.7% to 28.9%, respectively, suggesting that these N-containing groups serve as adsorption sites. Additionally, −NH− can also reduce Cr(VI) to Cr(III). The O 1 s spectrum of BC-P*m*PD was divided into three peaks: Metal-O (531.2 eV), C=O (532.0 eV), and C–OH (533.1 eV) (Liu et al. 2022). After adsorption, the Metal-O and C–OH peak areas decreased from 47.4% to 31.7%, and 21.1% to 19.1%, respectively, while the C=O peak area increased from 31.6% to 49.2%. This indicates the involvement of these two groups in Cr(VI) removal, and active phenol groups could also contribute to Cr(VI) reduction (Zhao et al. 2021b). These changes for N and O containing groups were consistent with the FTIR spectra results.

To further confirm the reduction mechanisms, environmentally persistent free radicals (EPFRs) were monitored on the surface of BC-P*m*PD through ESR measurements to compare changes before and after Cr(VI) treatment and to investigate the role of EPFRs in Cr(VI) removal. As shown in Fig. 7g, the surface ESR signal of BC-P*m*PD significantly reduced after treatment with Cr(VI) (500 mg L^{-1}, 24 h), similar to previous findings (Zhao et al. 2018). This confirms the presence of EPFRs on the BC-P*m*PD surface and their depletion upon removal of Cr(VI) under acidic conditions. The spectral splitting factor (g-value) of BC-P*m*PD before and after Cr(VI) treatment was 2.005 and 2.004, respectively, indicating the presence of oxygen-centered radicals, particularly semiquinone radicals. Studies have shown that EPFRs can participate in the redox transformation of heavy metals and contribute to the reduction of Cr(VI) to Cr(III) (Zhang et al. 2023; Zhao et al. 2018). Therefore, it can be inferred that the EPFRs on BC-P*m*PD play a role in providing direct electrons and contributing to the reduction of Cr(VI) to Cr(III).

In order to quantify the contribution of EPFRs in BC-P*m*PD to the Cr(VI) reduction reaction, H_2O_2 was used to inhibit EPFRs (Fang et al. 2014). As shown in Additional file 1: Fig. S8, with an increase in H_2O_2 concentration, the removal efficiency initially decreased and thenincreased, with a maximum inhibition rate of 100%. This indicates that the adsorbed Cr(VI) in BC-P*m*PD was reduced by EPFRs. Thus, the reduction of Cr(VI) by amino and oxygen-containing functional groups could be neglected. Oxalyl chloride ($C_2Cl_2O_2$) was used as an amino and hydroxyl scavenger to quantify their contributions. The reaction of chloride with amine forms an amide, and DFT calculations in the previous literature confirm that the amide does not react with the Cr anion (Zhao et al. 2021b), enabling quantification of the amino group's contribution to Cr(VI) removal after *in-situ* locking. As shown in Additional file 1: Fig. S9, with an increase in the mass ratio of oxalyl chloride, the removal efficiency of Cr(VI) significantly decreased, ultimately converging to 4.24%. Subsequently, formaldehyde (HCHO) solution was used to hinder the reduction of Cr(VI) by phenolic hydroxyl (Zhao et al. 2021b). As shown in Additional file 1: Fig. S10, with an appropriate increase in the concentration of formaldehyde solution, the removal efficiency of Cr(VI) kept almost the same and contribution of Cr(VI) by the hydroxyl group of BC-P*m*PD was only 2.66%. By calculating the difference, the contribution of amino group was about 93.0%. This indicates that the amino group adsorbs most of $HCrO_4^-$ on the material's surface.

By further using the DFT calculation, the interaction energies of BC-P*m*PD and $HCrO_4^-$ in several different cases were obtained. As shown in Fig. 8a, b, the interaction energies of two O atoms in $HCrO_4^-$ with three or two H atoms in neutral 4a,5,10,10a-tetrahydro-phenazine-2,7-diamine molecule were −1.75 and −1.88 kcal mol^{-1} by forming three and two H bonds, respectively. Interestingly, when the $-NH_2$ in BC-P*m*PD was protonated (Fig. 8c), and its binding ability to the H atom in

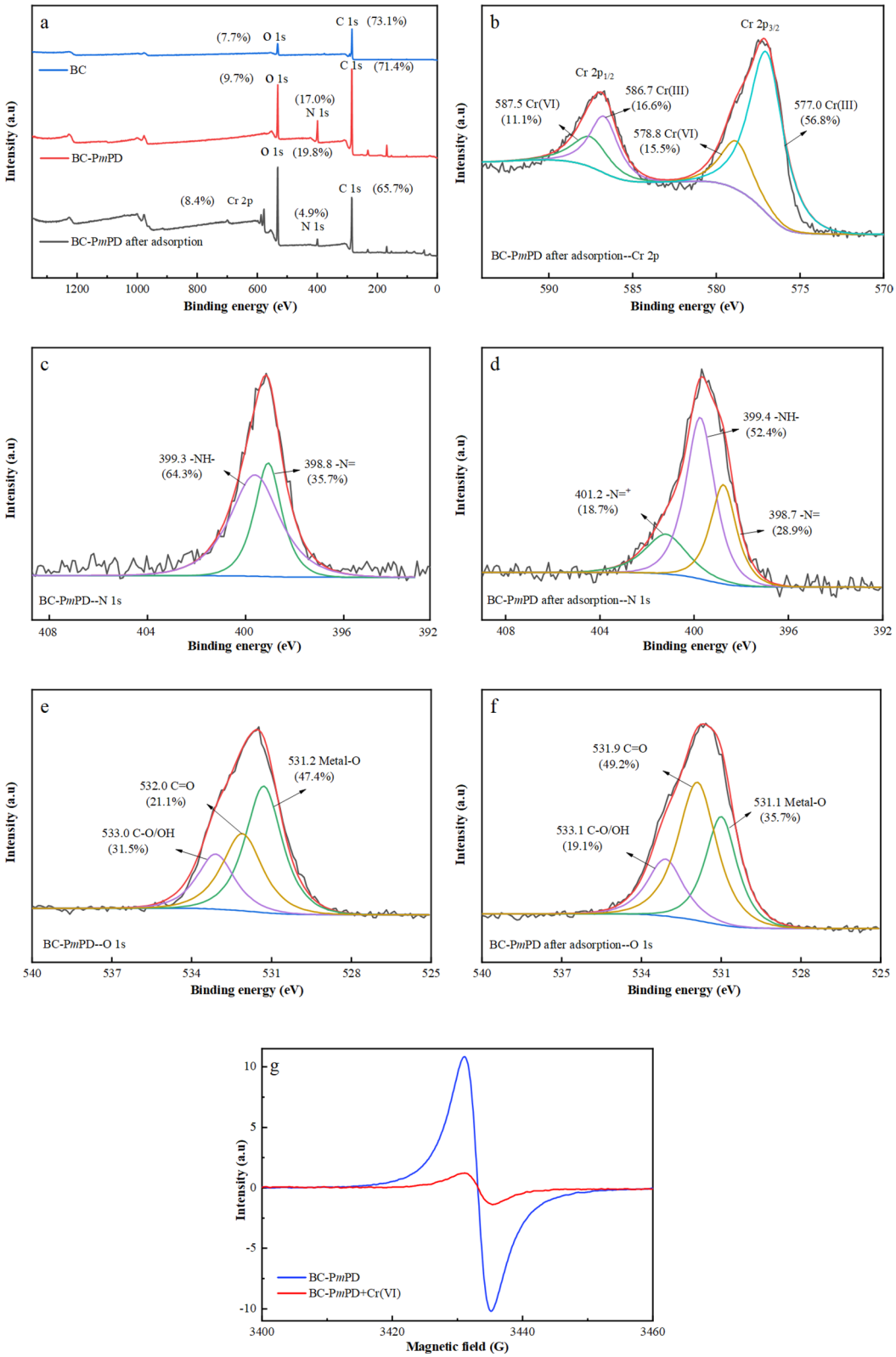

Fig. 7 **a** XPS spectra of BC, BC-P*m*PD before and after Cr(VI) removal, **b** XPS Cr 2p spectra of BC-P*m*PD after Cr(VI) removal, **c** XPS N 1 s spectra of BC-P*m*PD before and **d** after Cr(VI) removal, **e** XPS O 1 s spectra of BC-P*m*PD before and **f** after Cr(VI) removal, **g** ESR spectra of BC-P*m*PD before and after the removal of Cr(VI) (Concentrations: 500 mg L^{-1}, pH = 2, T = 30 °C, t = 24 h)

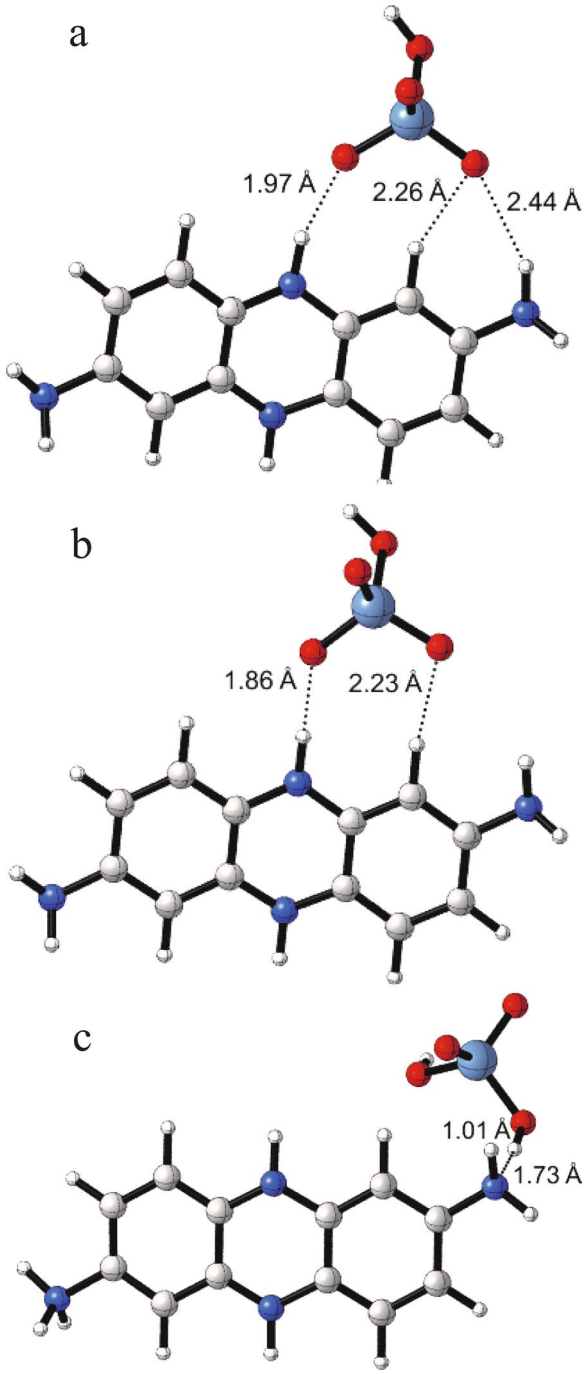

Fig. 8 Geometry-optimized structure for the interaction energy between BC-P*m*PD and $HCrO_4^-$ in several different cases. The interaction energy between **a** –NH– and $–NH_2$, **b** –NH–, **c** $–NH_2$ and $HCrO_4^-$ in the case of protonation. The spheres with gray, white, blue, red and light bule colors represent C, H, N, O, and Cr, respectively. (For interpretation of the references to color in this figure legend, the reader is referred to the web version of this article)

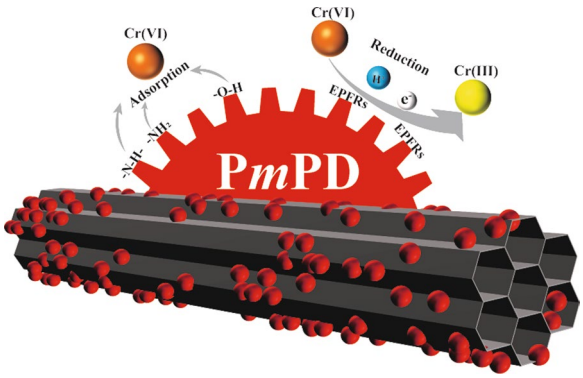

Fig. 9 The mechanistic schematic diagram of Cr(VI) removal by BC-P*m*PD

$HCrO_4^-$ was greatly improved (−7.55 kcal mol^{-1}). Proton transfer happened in an acidic environment before the formation of H bond.

Combining the results of FTIR, XPS, ESR analyses and the observation of Cr(III) concentration in the solution, the possible removal mechanisms can be proposed. The removal process of Cr(VI) anion on BC-P*m*PD was complex, involving electrostatic adsorption, proton transfer, H bond interaction, and reduction, and the removal mechanisms are described in Fig. 9. In acidic systems, $HCrO_4^-$ initially binds to BC-P*m*PD through electrostatic interaction between the protonated amino group on BC-P*m*PD. Subsequently, proton transfer occurred and H bond was formed. At last, all the adsorbed Cr(VI) at the beginning of the reaction is rapidly reduced to Cr(III) by EPFRs.

3.6 Recycle and desorption

To assess the practical applicability of BC-P*m*PD, desorption experiments were conducted using various solutions. Noticeable differences were observed in the desorption capabilities of four distinct analytical solutions (Additional file 1: Fig. S11a). The desorption rates followed this sequence: deionized water < HCl < ethylenediaminetetraacetic acid (EDTA) < NaOH. Notably, the desorption rate for NaOH was remarkably high at 93.2%. However, it was only 1.38%, 3.01%, and 14.2% for deionized water, HCl, and weakly basic EDTA, respectively. The previous studies also suggested that NaOH had a better desorption capacity (Shi et al. 2018; Xiao et al. 2019; Zhang et al. 2016). These findings demonstrate that BC-P*m*PD can be efficiently regenerated in an alkaline solution, because OH^- replaced Cr(VI) through ion exchange. This property enables the cyclic utilization of BC-P*m*PD for Cr(VI) adsorption. Conversely, acidic conditions are unfavorable for Cr(VI) desorption, as only a small portion of Cr(VI) could be dissolved.

The stability and reusability of BC-P*m*PD determine its potential viability in wastewater treatment. The adsorption–desorption process was repeated for five cycles, and its impact on Cr(VI) removal is presented in Additional file 1: Fig. S11b. The initial Cr(VI) adsorption capacity was 638 mg g^{-1}, which decreased by 32.0% after the second cycle due to irreversible redox reactions post the initial adsorption (Hao et al. 2021). The cumulative removal amount of Cr(VI) was high up to 1988 mg g^{-1} over five cycles. These results indicate that BC-P*m*PD's adsorption–desorption capacity for Cr(VI) exceeds that of core–shell magnetic Fe_3O_4@poly(*m* phenylenediamine) particles, even after five cycles (Wang et al. 2015b). Overall, BC-P*m*PD provides more adsorption sites and effective recovery of occupied adsorption sites (Dognani et al. 2019). Nevertheless, after the fifth usage of BC-P*m*PD, the removal amount reduced by 65.8% as compared to the first usage. Thus, further exploration of improved desorption agents is essential to achieve complete recovery of the reducing species on BC-P*m*PD in the future study.

3.7 Application of BC-P*m*PD in electroplating wastewater treatment

To expand the application scope of BC-P*m*PD, treatment of actual electroplating wastewater containing 200 mg L^{-1} Cr(VI) was conducted. After 5 h of reaction with the electroplating wastewater, BC-P*m*PD removed 98.5% of Cr(VI), slightly faster and more efficiently than the simulated wastewater (Additional file 1: Fig. S12a). This enhancement may result from the presence of Cl^- and SO_4^{2-}, which can promote Cr(VI) removal (Yang and Jiang 2014; Zhao et al. 2021a). Despite the presence of Cu^{2+}, Zn^{2+}, and Cd^{2+}, no competition with $HCrO_4^-$ occurred, indicating BC-P*m*PD's selectivity for Cr(VI) removal in practical scenarios. At the same time, Cr(III) was produced in electroplating wastewater, demonstrating that reduction also occurred to decrease the toxicity of Cr(VI) (Additional file 1: Fig. S12b). Based on the above analysis, BC-P*m*PD exhibited promising potential for treating highly concentrated Cr(VI) polluted electroplating wastewater.

4 Conclusions

In this study, a novel 3D composite, BC-P*m*PD, was developed for Cr(VI) removal. The removal performance of BC-P*m*PD in solution correlated closely with initial temperature, concentration, and pH. Its maximum equilibrium adsorption capacity for Cr(VI) reached 775 mg g^{-1} at 303 K, significantly higher than that of bare BC and P*m*PD. This substantial improvement in Cr(VI) removal efficiency was due to the adsorbent's spontaneous and heat-absorbing adsorption process. XPS, FTIR, and ESR spectroscopy revealed that the removal process involved chemical electrostatic adsorption and reduction reactions between Cr(VI) and protonated amino groups. DFT calculation confirmed proton transfer occurred between protonated $-NH_2$ and $HCrO_4^-$ before formation of H bond. The role of EPFRs in BC-P*m*PD's ability to reduce Cr(VI) was also highlighted. The contributions of amino and hydroxyl groups were demonstrated. The aforementioned experimental results underscore BC-P*m*PD's merits, including high removal capacity, stability, and reusability. This composite presented a simple and efficient strategy for removing Cr(VI) from electroplating wastewater by combining P*m*PD's high Cr(VI) adsorption capacity with the accessibility and affordability of BC.

Supplementary Information

The online version contains supplementary material available at https://doi.org/10.1007/s42773-024-00338-x.

Additional file 1.

Additional file 2.

Acknowledgements
We would like to thank the National Natural Science Foundation of China (42377038, 41920104003), Guangdong Provincial Key Laboratory of Environmental Pollution Control and Remediation Technology (2020B1212060022), and GDAS' Project of Science and Technology Development (2023GDASZH-2023010103).

Author contributions
All authors contributed to the study conception and design. Qiu Rongliang: Conceptualization, Editing and Supervision. Wu Zhiguo: Reviewing and Editing. Yang Zongzheng: Writing-Reviewing-Manuscript modification. Wang Jinjin: Writing-Data Collection-Experimental Investigation. Zhao Nan: Review-manuscript modification-Theoretical supplement. Pang Runyi: Writing-Original draft preparation. Zhao Chuanfang: Conducting DFT computations. Deng Ying: Data and manuscript correction. Di Yang: Experimental Investigation. Jiang Haochen: Practice.

Funding
This work was supported by National Natural Science Foundation of China (42377038, 41920104003), the Research Fund Program of Guangdong Provincial Key Laboratory of Environmental Pollution Control and Remediation Technology (2020B1212060022), and GDAS' Project of Science and Technology Development (2023GDASZH-2023010103).

Availability of data and materials
The datasets used or analyzed during the current study are available from the corresponding author on reasonable request.

Declarations

Ethics approval and consent to participate
Not applicable.

Competing interests
The authors declare that they have no known competing financial interests or personal relationships that could have appeared to influence the work reported in this paper. The corresponding author is submitting the paper on behalf of all the co-authors.

Author details
[1]College of Oceanography and Environment, Tianjin University of Science and Technology, Tianjin 300457, China. [2]College of Chemical Engineering and Materials, Tianjin University of Science and Technology, Tianjin 300457, China. [3]National-Regional Joint Engineering Research Center for Soil Pollution Control and Remediation in South China, Guangdong Key Laboratory of Integrated Agro-Environmental Pollution Control and Management, Institute of Eco-Environmental and Soil Sciences, Guangdong Academy of Sciences, Guangzhou 510650, China. [4]Guangdong Provincial Key Laboratory of Environmental Pollution Control and Remediation Technology, School of Environmental Science and Engineering, Sun Yat-Sen University, Guangzhou 510275, China. [5]Guangdong Laboratory for Lingnan Modern Agriculture, College of Natural Resources and Environment, South China Agricultural University, Guangzhou 510642, China. [6]Research Center for Eco-Environmental Sciences, Chinese Academy of Sciences, Beijing 100085, China.

Received: 19 November 2023 Revised: 27 April 2024 Accepted: 29 April 2024
Published online: 16 May 2024

References

Albadarin AB, Mangwandi C et al (2012) Modelling and fixed bed column adsorption of Cr(VI) onto orthophosphoric acid-activated lignin. Chin J Chem Eng 20(3):469–477. https://doi.org/10.1016/s1004-9541(11)60208-5

Al-Ghouti MA, Da'ana DA (2020) Guidelines for the use and interpretation of adsorption isotherm models: a review. J Hazard Mater 393:122383. https://doi.org/10.1016/j.jhazmat.2020.122383

Andrae DH, Dolg M, Stoll H, Preuss H (1991) Energy-adjustedab initio pseudopotentials for the second and third row transition elements Molecular test for M2 (M=Ag, Au) and MH (M=Ru, Os). Theor Chim Acta 78:247–266. https://doi.org/10.1007/BF01114537

Asuquo E, Martin A, Nzerem P, Siperstein F, Fan X (2017) Adsorption of Cd(II) and Pb(II) ions from aqueous solutions using mesoporous activated carbon adsorbent: equilibrium, kinetics and characterisation studies. J Environ Chem Eng 5(1):679–698. https://doi.org/10.1016/j.jece.2016.12.043

Becke AD (1993a) Density-functional thermochemistry. III. The role of exact exchange. The J Chem Phys 98(7):5648–5652. https://doi.org/10.1063/1.464913

Becke AD (1993b) A new mixing of Hartree-Fock and local density-functional theories. J Chem Phys 98(2):1372–1377. https://doi.org/10.1063/1.464304

Bhaumik M, Maity A, Srinivasu VV, Onyango MS (2012) Removal of hexavalent chromium from aqueous solution using polypyrrole-polyaniline nanofibers. Chem Eng J 181–182:323–333. https://doi.org/10.1016/j.cej.2011.11.088

Binish CJ, Vijayasankar AV, Aan MPS (2022) Synthesis and characterization of Poly-Vinyl Alcohol-Alumina composite film: An efficient adsorbent for the removal of Chromium (VI) from water. Mater Today 62:5182–5188. https://doi.org/10.1016/j.matpr.2022.02.629

Cao E, Duan W, Yi L, Wang A, Zheng Y (2017) Poly(m -phenylenediamine) functionalized *Calotropis gigantea* fiber for coupled adsorption reduction for Cr(VI). J Mol Liq 240:225–232. https://doi.org/10.1016/j.molliq.2017.05.087

Chen Y, Xu S, Han S, Chu S, Yang L, Jiang C (2019) Reusable and removable PmPD/PVA membrane for effective Cr(vi) adsorption and reduction. New J Chem 43(13):5039–5046. https://doi.org/10.1039/c8nj06166a

Chen M, Chen X, Xu X, Xu Z, Zhang Y, Song B, Tsang DCW, Xu N, Cao X (2022) Biochar colloids facilitate transport and transformation of Cr(VI) in soil: active site competition coupling with reduction reaction. J Hazard Mater. https://doi.org/10.1016/j.jhazmat.2022.129691

Clark TC et al (1983) Efficient diffuse function-augmented basis sets for anion calculations. J Comput Chem 4:294–301. https://doi.org/10.1002/jcc.540040303

Ding J, Pu L, Wang Y, Wu B, Yu A, Zhang X, Pan B, Zhang Q, Gao G (2018) Adsorption and reduction of Cr(VI) together with Cr(III) sequestration by polyaniline confined in pores of polystyrene beads. Environ Sci Technol 52(21):12602–12611. https://doi.org/10.1021/acs.est.8b02566

Dognani G, Hadi P, Ma H, Cabrera FC, Job AE, Agostini DLS, Hsiao BS (2019) Effective chromium removal from water by polyaniline-coated electrospun adsorbent membrane. Chem Eng J 372:341–351. https://doi.org/10.1016/j.cej.2019.04.154

Dong X, Ma LQ, Li Y (2011) Characteristics and mechanisms of hexavalent chromium removal by biochar from sugar beet tailing. J Hazard Mater 190(1–3):909–915. https://doi.org/10.1016/j.jhazmat.2011.04.008

El-Barbary AAA, Alkhateeb MA (2021) DFT Study of Se-doped nanocones as highly efficient hydrogen storage carrier. Graphene 10(04):49–60. https://doi.org/10.4236/graphene.2021.104004

Fang G, Gao J, Liu C, Dionysiou DD, Wang Y, Zhou D (2014) Key role of persistent free radicals in hydrogen peroxide activation by biochar: implications to organic contaminant degradation. Environ Sci Technol 48(3):1902–1910. https://doi.org/10.1021/es4048126

Feller D (1996) The role of databases in support of computational chemistry calculations. J Comput Chem 17:1571–1586

Gao K, Li J, Chen M, Jin Y, Ma Y, Ou G, Wei Z (2021) ZIF-67 derived magnetic nanoporous carbon coated by poly(m-phenylenediamine) for hexavalent chromium removal. Sep Purif Technol 277:119436. https://doi.org/10.1016/j.seppur.2021.119436

Guo X, Xue Y, Zheng R, Chen S, Xue W, Lan X, Wang L, Xiao H (2023) Zwitterionic doxorubicin loaded micelles based on polyethyleneimine for enhanced antitumor therapy in vivo. New J Chem 47(24):11636–11642. https://doi.org/10.1039/d3nj01011b

Hao Y, Zhou Y, Xu N, Tian K, Liang P, Jiang H (2021) ZIF-8 modulated synthesis of iron oxide @ poly(m-phenylenediamine) (Z) particles (Fe3O4@PmPD(Z)) for the removal of Cr(VI) from wastewater. Synth Met 282:116960. https://doi.org/10.1016/j.synthmet.2021.116960

Hay PJ, Wadt WR (1985) Ab initio effective core potentials for molecular calculations. Potentials for K to Au including the outermost core orbitals. J Chem Phys 82(1):299–310. https://doi.org/10.1063/1.448975

Hu XJ, Wang JS, Liu YG, Li X, Zeng GM, Bao ZL, Zeng XX, Chen AW, Long F (2011) Adsorption of chromium (VI) by ethylenediamine-modified cross-linked magnetic chitosan resin: isotherms, kinetics and thermodynamics. J Hazard Mater 185(1):306–314. https://doi.org/10.1016/j.jhazmat.2010.09.034

Huang MR, Lu HJ, Li XG (2007) Efficient multicyclic sorption and desorption of lead ions on facilely prepared poly(m-phenylenediamine) particles with extremely strong chemoresistance. J Colloid Interface Sci 313(1):72–79. https://doi.org/10.1016/j.jcis.2007.04.024

Jin L, Huang L, Ren L, He Y, Tang J, Wang S, Yang W, Wang H, Chai L (2018) Preparation of stable and high-efficient poly(m-phenylenediamine)/reduced graphene oxide composites for hexavalent chromium removal. J Mater Sci 54(1):383–395. https://doi.org/10.1007/s10853-018-2844-9

Kera NH, Bhaumik M, Pillay K, Ray SS, Maity A (2018) m-Phenylenediamine-modified polypyrrole as an efficient adsorbent for removal of highly toxic hexavalent chromium in water. MaterToday Commun 15:153–164. https://doi.org/10.1016/j.mtcomm.2018.02.033

Lee C, Yang W, Parr RG (1988) Development of the Colle-Salvetti correlation-energy formula into a functional of the electron density. Phys Rev B Condens Matter 37(2):785–789. https://doi.org/10.1103/physrevb.37.785

Legault CY (2009) CYLview. 1.0b ed., Université de Sherbrooke.

Li X-G, Huang M-R, Li S-X (2004) Facile synthesis of poly(1,8-diaminonaphthalene) microparticles with a very high silver-ion adsorbability by a chemical oxidative polymerization. Acta Mater 52(18):5363–5374. https://doi.org/10.1016/j.actamat.2004.07.042

Liu Y, Liu F, Ding N, Shen C, Li F, Dong L, Huang M, Yang B, Wang Z, Sand W (2019) Boosting Cr(VI) detoxification and sequestration efficiency with carbon nanotube electrochemical filter functionalized with nanoscale polyaniline: performance and mechanism. Sci Total Environ 695:133926. https://doi.org/10.1016/j.scitotenv.2019.133926

Liu K, Zheng F, Xiao Y, Fang J, Zhao C, Zhao N, Zhao C, Zhang W, Zhang W, Qiu R (2022) High Fe utilization efficiency and low toxicity of Fe3C@Fe0 loaded biochar for removing of tetracycline hydrochloride in wastewater. J Clean Prod 353:131630. https://doi.org/10.1016/j.jclepro.2022.131630

Liu K, Zhao D, Hu Z, Xiao Y, He C, Jiang F, Zhao N, Zhao C, Zhang W, Qiu R (2023) The adsorption and reduction of anionic Cr(VI) in groundwater by novel iron carbide loaded on N-doped carbon nanotubes: Effects of Fe-confinement. Chem Eng J 452:139357. https://doi.org/10.1016/j.cej.2022.139357

Ma Y, Liu WJ, Zhang N, Li YS, Jiang H, Sheng GP (2014) Polyethylenimine modified biochar adsorbent for hexavalent chromium removal from the aqueous solution. Bioresour Technol 169:403–408. https://doi.org/10.1016/j.biortech.2014.07.014

Miertuš SS, Tomasi J (1981) Electrostatic interaction of a solute with a continuum. A direct utilizaion of AB initio molecular potentials for the prevision of solvent effects. Chem Phys 55:117–129. https://doi.org/10.1016/0301-0104(81)85090-2

Peng Z, Zhao H, Lyu H, Wang L, Huang H, Nan Q, Tang J (2018) UV modification of biochar for enhanced hexavalent chromium removal from aqueous solution. Environ Sci Pollut Res Int 25(11):10808–10819. https://doi.org/10.1007/s11356-018-1353-3

Qian L, Long Y, Li H, Wei Z, Liang C, Liu R, Chen M (2023) Unveiling the role of biochar in simultaneous removal of hexavalent chromium and trichloroethylene by biochar supported nanoscale zero-valent iron. Sci Total Environ. https://doi.org/10.1016/j.scitotenv.2023.164243

Rafique MI, Usman ARA, Ahmad M, Al-Wabel MI (2021) Immobilization and mitigation of chromium toxicity in aqueous solutions and tannery waste-contaminated soil using biochar and polymer-modified biochar. Chemosphere 266:129198. https://doi.org/10.1016/j.chemosphere.2020.129198

Shaheen SM, Mosa A et al (2022) Removal of toxic elements from aqueous environments using nano zero-valent iron- and iron oxide-modified biochar: a review. Biochar. https://doi.org/10.1007/s42773-022-00149-y

Shan R, Shi Y, Gu J, Bi J, Yuan H, Luo B, Chen Y (2020) Aqueous Cr(VI) removal by biochar derived from waste mangosteen shells: Role of pyrolysis and modification on its absorption process. J Environ Chem Eng 8(4):103885. https://doi.org/10.1016/j.jece.2020.103885

Shi S, Yang J, Liang S, Li M, Gan Q, Xiao K, Hu J (2018) Enhanced Cr(VI) removal from acidic solutions using biochar modified by Fe3O4@SiO2-NH2 particles. Sci Total Environ 628–629:499–508. https://doi.org/10.1016/j.scitotenv.2018.02.091

Sinha R, Kumar R, Abhishek K, Shang J, Bhattacharya S, Sengupta S, Kumar N, Singh RK, Mallick J, Kar M, Sharma P (2022) Single-step synthesis of activated magnetic biochar derived from rice husk for hexavalent chromium adsorption: equilibrium mechanism, kinetics, and thermodynamics analysis. Groundw Sustain Dev 18:100796. https://doi.org/10.1016/j.gsd.2022.100796

Song J, He Q, Hu X, Zhang W, Wang C, Chen R, Wang H, Mosa A (2019) Highly efficient removal of Cr(VI) and Cu(II) by biochar derived from *Artemisia argyi* stem. Environ Sci Pollut Res Int 26(13):13221–13234. https://doi.org/10.1007/s11356-019-04863-2

Song J, Messele SA, Meng L, Huang Z, Gamal El-Din M (2021) Adsorption of metals from oil sands process water (OSPW) under natural pH by sludge-based Biochar/Chitosan composite. Water Res 194:116930. https://doi.org/10.1016/j.watres.2021.116930

Stephens PJD et al (1994) Ab initio calculation of vibrational absorption and circular dichroism spectra using density functional force fields. J Phys Chem 98:11623–11627. https://doi.org/10.1016/0009-2614(94)00605-9

Stoica-Guzun A, Stroescu M, Jinga SI, Mihalache N, Botez A, Matei C, Berger D, Damian CM, Ionita V (2016) Box-Behnken experimental design for chromium(VI) ions removal by bacterial cellulose-magnetite composites. Int J Biol Macromol 91:1062–1072. https://doi.org/10.1016/j.ijbiomac.2016.06.070

Tian X, Wang W, Wang Y, Komarneni S, Yang C (2015) Polyethylenimine functionalized halloysite nanotubes for efficient removal and fixation of Cr (VI). Microporous Mesoporous Mat 207:46–52. https://doi.org/10.1016/j.micromeso.2014.12.031

Tripathy S, Sahu S, Patel RK, Panda RB, Kar PK (2021) Efficient removal of Cr(VI) by polyaniline modified biochar from date (*Phoenix dactylifera*) seed. Groundw Sustain Dev 15:100653. https://doi.org/10.1016/j.gsd.2021.100653

Wan Z, Li M, Zhang Q, Fan Z, Verpoort F (2018) Concurrent reduction-adsorption of chromium using m-phenylenediamine-modified magnetic chitosan: kinetics, isotherm, and mechanism. Environ Sci Pollut Res Int 25(18):17830–17841. https://doi.org/10.1007/s11356-018-1941-2

Wang H, Yuan X, Wu Y, Chen X, Leng L, Wang H, Li H, Zeng G (2015a) Facile synthesis of polypyrrole decorated reduced graphene oxide–Fe3O4 magnetic composites and its application for the Cr(VI) removal. Chem Eng J 262:597–606. https://doi.org/10.1016/j.cej.2014.10.020

Wang T, Zhang L, Li C, Yang W, Song T, Tang C, Meng Y, Dai S, Wang H, Chai L, Luo J (2015b) Synthesis of core-shell magnetic Fe3O4@poly(m-Phenylenediamine) particles for chromium reduction and adsorption. Environ Sci Technol 49(9):5654–5662. https://doi.org/10.1021/es5061275

Wang Y, Yang Q, Chen J, Yang J, Zhang Y, Chen Y, Li X, Du W, Liang A, Ho SH, Chang JS (2020) Adsorption behavior of Cr(VI) by magnetically modified *Enteromorpha prolifera* based biochar and the toxicity analysis. J Hazard Mater 395:122658. https://doi.org/10.1016/j.jhazmat.2020.122658

Xiao F, Cheng J, Cao W, Yang C, Chen J, Luo Z (2019) Removal of heavy metals from aqueous solution using chitosan-combined magnetic biochars. J Colloid Interface Sci 540:579–584. https://doi.org/10.1016/j.jcis.2019.01.068

Xu X, Huang H, Zhang Y, Xu Z, Cao X (2019a) Biochar as both electron donor and electron shuttle for the reduction transformation of Cr(VI) during its sorption. Environ Pollut 244:423–430. https://doi.org/10.1016/j.envpol.2018.10.068

Xu Y, Chen J, Chen R, Yu P, Guo S, Wang X (2019b) Adsorption and reduction of chromium(VI) from aqueous solution using polypyrrole/calcium rectorite composite adsorbent. Water Res 160:148–157. https://doi.org/10.1016/j.watres.2019.05.055

Xu Z, Wan Z, Sun Y, Gao B, Hou D, Cao X, Komárek M, Ok YS, Tsang DCW (2022) Electroactive Fe-biochar for redox-related remediation of arsenic and chromium: distinct redox nature with varying iron/carbon speciation. J Hazard Mater. https://doi.org/10.1016/j.jhazmat.2022.128479

Xu Z, Sun M, Xu X, Cao X, Ippolito JA, Mohanty SK, Ni B-J, Xu S, Tsang DCW (2023) Electron donation of Fe-Mn biochar for chromium(VI) immobilization: Key roles of embedded zero-valent iron clusters within iron-manganese oxide. J Hazard Mater. https://doi.org/10.1016/j.jhazmat.2023.131632

Yang GX, Jiang H (2014) Amino modification of biochar for enhanced adsorption of copper ions from synthetic wastewater. Water Res 48:396–405. https://doi.org/10.1016/j.watres.2013.09.050

Yang Z, Ren L, Jin L, Huang L, He Y, Tang J, Yang W, Wang H (2018) In-situ functionalization of poly(m-phenylenediamine) nanoparticles on bacterial cellulose for chromium removal. Chem Eng J 344:441–452. https://doi.org/10.1016/j.cej.2018.03.086

Yuan X, Cao Y, Li J, Patel AK, Dong C-D, Jin X, Gu C, Yip ACK, Tsang DCW, Ok YS (2023) Recent advancements and challenges in emerging applications of biochar-based catalysts. Biotechnol Adv. https://doi.org/10.1016/j.biotechadv.2023.108181

Zhang N, Zang G-L, Shi C, Yu H-Q, Sheng G-P (2016) A novel adsorbent TEMPO-mediated oxidized cellulose nanofibrils modified with PEI: preparation, characterization, and application for Cu(II) removal. J Hazard Mater 316:11–18. https://doi.org/10.1016/j.jhazmat.2016.05.018

Zhang X, Fu W, Yin Y, Chen Z, Qiu R, Simonnot MO, Wang X (2018) Adsorption-reduction removal of Cr(VI) by tobacco petiole pyrolytic biochar: batch experiment, kinetic and mechanism studies. Bioresour Technol 268:149–157. https://doi.org/10.1016/j.biortech.2018.07.125

Zhang Y, He R, Zhao J (2023) Removal mechanism of tetracycline-Cr(VI) combined pollutants by different S-doped sludge biochars: role of environmentally persistent free radicals. Chemosphere 317:137856. https://doi.org/10.1016/j.chemosphere.2023.137856

Zhao N, Lv Y, Yang X, Huang F, Yang J (2017) Characterization and 2D structural model of corn straw and poplar leaf biochars. Environ Sci Pollut Res 25(26):25789–25798. https://doi.org/10.1007/s11356-017-0959-1

Zhao N, Yin Z, Liu F, Zhang M, Lv Y, Hao Z, Pan G, Zhang J (2018) Environmentally persistent free radicals mediated removal of Cr(VI) from highly saline water by corn straw biochars. Bioresour Technol 260:294–301. https://doi.org/10.1016/j.biortech.2018.03.116

Zhao N, Zhao C, Liu K, Zhang W, Tsang DCW, Yang Z, Yang X, Yan B, Morel JL, Qiu R (2021a) Experimental and DFT investigation on N-functionalized biochars for enhanced removal of Cr(VI). Environ Pollut 291:118244. https://doi.org/10.1016/j.envpol.2021.118244

Zhao N, Zhao C, Tsang DCW, Liu K, Zhu L, Zhang W, Zhang J, Tang Y, Qiu R (2021b) Microscopic mechanism about the selective adsorption of Cr(VI) from salt solution on O-rich and N-rich biochars. J Hazard Mater 404(Pt A):124162. https://doi.org/10.1016/j.jhazmat.2020.124162

Zhao N, Tan X, Xiong J, Chen N, Gao J, Wang R, Yang X, Zhang W, Zhang W, Qiu R (2022a) Quantitative analysis on the redox conversion mechanism of Cr(VI) and As(III) by iron carbide based biochar composites. Chem Eng J 446:137417. https://doi.org/10.1016/j.cej.2022.137417

Zhao R, Wang B, Zhang X, Lee X, Chen M, Feng Q, Chen S (2022b) Insights into Cr(VI) removal mechanism in water by facile one-step pyrolysis prepared coal gangue-biochar composite. Chemosphere 299:134334. https://doi.org/10.1016/j.chemosphere.2022.134334

Zhu X, Labianca C, He M, Luo Z, Wu C, You S, Tsang DCW (2022) Life-cycle assessment of pyrolysis processes for sustainable production of biochar from agro-residues. Bioresour Technol. https://doi.org/10.1016/j.biortech.2022.127601

Zou H, Zhao J, He F, Zhong Z, Huang J, Zheng Y, Zhang Y, Yang Y, Yu F, Bashir MA, Gao B (2021) Ball milling biochar iron oxide composites for the removal of chromium (Cr(VI)) from water: performance and mechanisms. J Hazard Mater 413:125252. https://doi.org/10.1016/j.jhazmat.2021.125252